PHYSICAL REVIEW B **104**, 184514 (2021)

Magnetoconductance and photoresponse properties of disordered NbTiN films

M. Sidorova,[1,2] A. D. Semenov,[2] H.-W. Hübers,[1,2] S. Gyger,[3] S. Steinhauer,[3] X. Zhang,[4,5] and A. Schilling[6]
[1]*Department of Physics, Humboldt-Universität zu Berlin, Newtonstrasse 15, 12489 Berlin, Germany*
[2]*Institute of Optical Sensor Systems, German Aerospace Center, Rutherfordstrasse 2, 12489 Berlin, Germany*
[3]*Department of Applied Physics, KTH Royal Institute of Technology, 106 91 Stockholm, Sweden*
[4]*State Key Laboratory of Functional Materials for Informatics, Shanghai Institute of Microsystem and Information Technology, Chinese Academy of Sciences, Shanghai 200050, China*
[5]*CAS Center for Excellence in Superconducting Electronics, Shanghai 200050, China*
[6]*Physics Institute, University of Zürich, Winterthurerstrasse 190, 8057 Zürich, Switzerland*

(Received 9 August 2021; accepted 11 November 2021; published 22 November 2021)

We report on the experimental study of phonon properties and electron-phonon scattering in thin superconducting NbTiN films, which are intensively exploited in various applications. Studied NbTiN films with sub-10-nm thicknesses are disordered with respect to electron transport, the Ioffe-Regel parameter of $k_F l_e =$ 2.5–3.0 (k_F is the Fermi wave vector, and l_e is the electron mean free path), the inelastic electron-phonon interaction, and the product $q_T l_e \ll 1$ (q_T is the wave vector of a thermal phonon). By means of magnetoconductance and photoresponse techniques, we derive the inelastic electron-phonon scattering rate $1/\tau_{e\text{-ph}}$ and determine sound velocities and phonon heat capacities. In the temperature range from 12 to 20 K, the scattering rate varies with temperature as $1/\tau_{e\text{-ph}} \propto T^{3.45\pm0.05}$; its value extrapolated to 10 K amounts to approximately 1/16 ps. Making a comparative analysis of our films and other films used in superconducting devices, such as polycrystalline granular NbN and amorphous WSi, we find a systematic reduction of the sound velocity in all these films by about 50% compared to the corresponding bulk crystalline materials. A corresponding increase in the phonon heat capacities in all these films is, however, less than the Debye model predicts. We attribute these findings to reduced film dimensionality and film morphology.

DOI: 10.1103/PhysRevB.104.184514

I. INTRODUCTION

Thin disordered NbTiN films are intensively exploited in various superconducting devices. They have become a prominent material for the fabrication of scientific and commercial superconducting nanowire single-photon detectors (SNSPDs) [1] and already a decade ago were considered an alternative to NbN films in hot-electron bolometers (HEBs) [2]. NbTiN is a potential alternative to Al for high-kinetic-inductance, low-loss microwave resonators [3,4] and a good candidate for Cooper-pair transistors [5]. Besides applied physics, NbTiN films are relevant for fundamental studies of disorder-driven effects in superconductors, e.g., superconductor-insulator [6] and Berezinskii-Kosterlitz-Thouless transitions [7].

Both electron transport properties and phonon-related properties of superconducting films are of high importance because they determine the performance metrics of practical devices. For instance, the rate of electron-phonon (*e*-ph) scattering and the sound velocity along with the heat capacity of phonons jointly control the relative strength of electron heating and the cooling rate of electrons and therefore limit the intermediate-frequency (IF) bandwidth in HEBs to just a few gigahertz [8,9] or impact the timing jitter in SNSPDs [10]. Although the literature has repeatedly indicated that NbN-based HEBs demonstrate larger IF bandwidths than NbTiN-based HEBs (see, e.g., the review in [2] and references therein), the explicit reason for this experimental fact has never been clarified. The lack of both theoretical and empirical descriptions of properties of NbTiN and other films used in superconducting devices is often caused by their complexity, i.e., the high level of disorder and reduced dimensionality with respect to different physical phenomena. NbTiN is a compound of two well-studied nitrides, NbN and TiN, with orders of magnitude different *e*-ph scattering times ($\tau_{e\text{-ph}} = 1.8$ ns for TiN [11] vs ~0.01 ns for NbN [12] at 10 K). From this perspective, it is interesting to understand whether the stoichiometry of $\mathrm{Nb}_x\mathrm{Ti}_{1-x}\mathrm{N}$ could be used for fine-tuning the $\tau_{e\text{-ph}}$ of the compound. The matter is even more complicated since the superconducting properties of NbN films alone, such as the transition temperature, resistivity, and critical current density, are strongly dependent on the film stoichiometry [13]. It has been shown that SNSPDs based on amorphous superconductors, e.g., silicides such as WSi [14] and MoSi [15], can show favorable properties for the detection of low-energy infrared photons due to their lower superconducting transition temperature compared to Nb-based materials. However, the explicit role, if any, of the amorphous state in this improvement remains unclear.

In this study, we derive various properties of NbTiN films at low temperatures, in particular, the *e*-ph scattering time, the sound velocity, and the phonon heat capacity, and carry out a comparative analysis with other films (NbN and WSi) that are

TABLE I. Transport and superconducting parameters of NbTiN films studied here and the parameters (taken from the literature) of three other (NbN and WSi) superconducting films. RRR is the ratio between resistances at 300 K and at 25 K. The values of k_F and l_e are computed from the carrier density n_e determined from Hall measurements at 25 K.

Film	Sample	d (nm)	RRR	T_{C0} (K)	R_{SN} (Ω/square)	D (cm^2/s)	$N(0)$ (J^{-1}m^{-3})	$B_{C2}(0)$ (T)	$\xi(0)$ (nm)	n_e (m^{-3})	k_F (nm^{-1})	l_e (nm)	$k_F l_e$
NbTiN	L135	6.0	0.80	8.41	710.6	0.458	2.00×10^{47}	13.9	4.9	4.97×10^{28}	11.4	0.22	2.5
NbTiN	L134	9.0	0.83	9.51	381.4	0.472	2.40×10^{47}	15.2	4.6	5.39×10^{28}	11.7	0.26	3.0
NbN[12]	2259	5.0	0.79	10.74	529.5	0.474	3.11×10^{47}	17.4	4.4				1.2[a]
NbN[12]	A853	6.4	0.71	8.35	954.0	0.339	1.89×10^{47}	19.2	4.2				0.9[a]
WSi[16]	4	5.0	0.96	4.08	357.0	0.700	3.10×10^{47}	6.7	7.0				1.8[a]

[a] For these films, the Ioffe-Regel parameter was computed as $k_F l_e = 3Dm_e/\hbar$ with the free-electron mass m_e.

intensively used in various superconducting devices. We show that, in all films, the sound velocity is reduced, and the phonon heat capacity is increased compared to the corresponding bulk crystalline materials. We suppose that this effect is exclusively controlled by modification of acoustic phonons due to reduced film dimensionality and variable film morphology.

II. EXPERIMENT AND RESULTS

NbTiN films with thicknesses of 6 and 9 nm (samples L135 and L134, respectively, in Table I) were deposited on 270-nm-thick SiO_2 layers thermally grown on Si substrates. Details of the deposition process were reported elsewhere [17]. According to studies of films prepared under the same sputtering conditions [18], the compositions of our $Nb_xTi_{1-x}N$ films had a Nb fraction of approximately $x = 0.6$ and a polycrystalline granular structure with diameters of most grains in the range from 4 to 5 nm.

A. Magnetotransport measurements

Resistance and Hall measurements were carried out by a standard four-probe technique on nonpatterned samples with a square geometry in a physical property measurement system (manufactured by Quantum Design) in magnetic fields applied perpendicular to the film surface. The van der Pauw method was used to determine the square resistance R_S and eliminate the effect of the planar geometry for two-dimensional (2D) specimens. Figure 1 shows the zero-field R_S as a function of temperature. When temperature decreases from 300 down to about 25 K, R_S increases and reaches a maximum value of 705.9 and 383.8 Ω/square for films with thicknesses of 6 and 9 nm, respectively, which is most likely due to Anderson localization. In the vicinity of superconducting transition, where the inequality $\ln(T/T_{C0}) \ll 1$ holds, we fitted the $R_S(T)$ data with the theory of fluctuation conductivity of Aslamazov and Larkin (AL) [19] and Maki and Thompson (MT) [20,21]. For 2D films, it is given by

$$R_S(T) = \left[\frac{1}{R_{\rm SN}} + A_{2d}\frac{1}{16}\frac{e^2}{\hbar \ln(T/T_{C0})}\right]^{-1}. \qquad (1)$$

Here, $\hbar$ is the reduced Planck constant, and e is the elementary charge; A_{2d} is a constant introduced to simplify the exact temperature-dependent MT term within the narrow temperature interval around T_{C0}. The best-fit values of the normal-state square resistance $R_{\rm SN}$ and the BCS mean-field transition temperature T_{C0} are listed in Table I; the best-fit values of A_{2d} are 2.21 and 2.16 for films with thicknesses of 6 and 9 nm, respectively.

An external magnetic field suppresses the superconducting transition, as shown in Fig. 2(a). From these measurements, we determined the temperature-dependent upper critical field $B_{C2}(T)$, shown in Fig. 2(b), as a preset field at the midpoint-transition temperature T_C, i.e., at the temperature where $R_S = R_{\rm SN}/2$. From the best linear fits of the experimental $B_{C2}(T)$ data at temperatures close to T_C (T/T_C between 0.05 and 0.25), we extracted the slopes dB_{C2}/dT. We further used them to compute the electron diffusion coefficient as $D = 4k_B/(\pi e)[dB_{C2}/dT]^{-1}$, the zero-temperature upper critical field as $B_{C2}(0) = -0.69T_{C0}dB_{C2}/dT$ for the dirty regime, and the zero-temperature Ginzburg-Landau coherence length $\xi(0) = \sqrt{\Phi_0/[2\pi B_{C2}(0)]}$, where k_B is the Boltzmann constant and $\Phi_0 = h/(2e)$ is the magnetic flux. The total electron density of states at the Fermi energy $N(0)$ was determined via the Einstein relation $N(0) = 1/(De^2R_{\rm SN}d)$, where d is the film thickness. All these parameters are listed in Table I.

The magnetic field dependence of the Hall voltage $V_H(B)$, i.e., the voltage appearing transverse to the current flow, is shown in Fig. 3. It was measured at 25 K, well above the superconducting transition, where $V_H(B)$ changes linearly with B. From the slope of the $V_H(B)$ dependence, we found the Hall coefficient $R_H = V_Hd/(IB)$, which provides us the carrier density n_e according to $R_H = -1/(n_e e)$. Further, knowing n_e, we determined the Fermi wave vector $k_F = (3\pi^2 n_e)^{1/3}$,

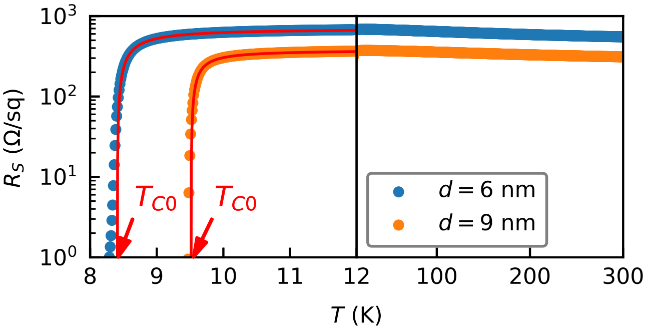

FIG. 1. Square resistance vs temperature at zero magnetic field (semilogarithmic scale). Symbols: experimental data; curves: the best fits obtained with Eq. (1) at temperatures where $\ln(T/T_{C0}) \ll 1$ and extrapolated to higher temperatures. The legend indicates film thicknesses.

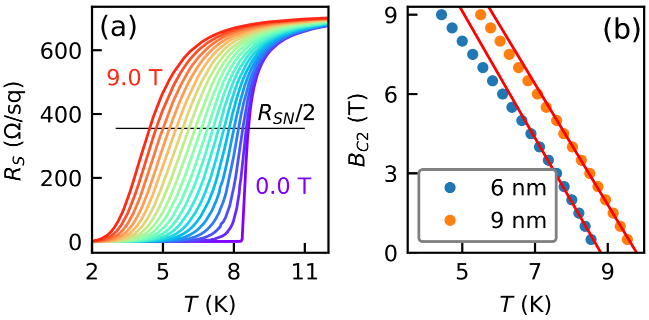

FIG. 2. (a) Square resistance vs temperature at a set of fixed magnetic fields in steps of 0.5 T for the representative NbTiN film with a thickness of 6 nm. The straight horizontal line drawn at $R_S = R_{SN}/2$ defines the midpoint transition temperature for each field. (b) Upper critical magnetic field as a function of temperature. The legend indicates film thicknesses. Symbols: experimental data; lines: the best linear fits, which are used to evaluate D and $B_{C2}(0)$.

the elastic electron mean free path $l_e = \hbar k_F/(n_e e^2 R_{SN} d)$, and, finally, the Ioffe-Regel parameter $k_F l_e$. The latter indicates a slightly different level of disorder in our films. All these parameters are listed in Table I.

B. Magnetoconductance

We determined the e-ph scattering time for our NbTiN films by means of the magnetoconductance technique described in [12]. We measured R_S, varying the magnetic field from 0 to 9 T at a set of fixed temperatures from 9 to 20 K. From these data, we computed the dimensionless magnetoconductance $\delta G(B, T) = 2\pi^2\hbar/e^2[R_S^{-1}(B, T) - R_S^{-1}(0, T)]$, plotted in Fig. 4. The change in the conductance induced by the magnetic field originates from quantum interference effects and is described by the theory of quantum corrections to conductivity (see Appendix A). We considered four quantum corrections given by Eqs. (A1)–(A4), which account for the electron weak-localization (WL) effect, AL and MT superconducting fluctuations, and electronic density of states (DOS) fluctuations. At experimental fields below $B_{C2}(0)$, the correction due to renormalization of the single-particle diffusion coefficient is small [22,23], and we neglect it.

We fitted the experimental $\delta G(B, T)$ data with a sum of Eqs. (A1)–(A4) using three independent fitting parameters, namely, the temperature-dependent electron dephasing time $\tau_\phi(T)$, the temperature-independent spin-orbit interaction time $\tau_{\rm so}$, and a constant C^*, allowing the latter to take values between 1.0 and 3.0 according to [24–27]. The best fits, shown with black curves in Fig. 4, were obtained with $C^* \approx 1.0$, $\tau_{\rm so} = 20 \pm 5$ ps, and a maximum $\tau_\phi(T)$ of about 4 ps. For both films, $\tau_{\rm so}$ is of the order of the maximum τ_ϕ, which corresponds to the weak spin-orbit interaction in our NbTiN films. The best-fit values of $\tau_\phi^{-1}(T)$ are plotted in Fig. 5(a).

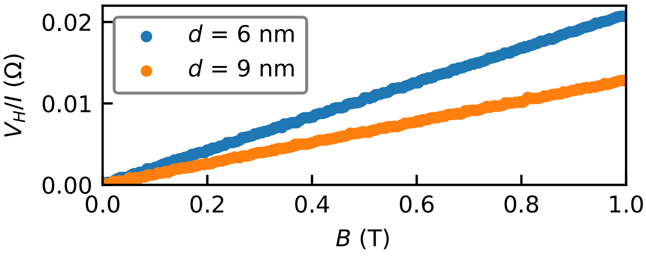

FIG. 3. Hall voltage divided by the transport current vs magnetic field at 25 K.

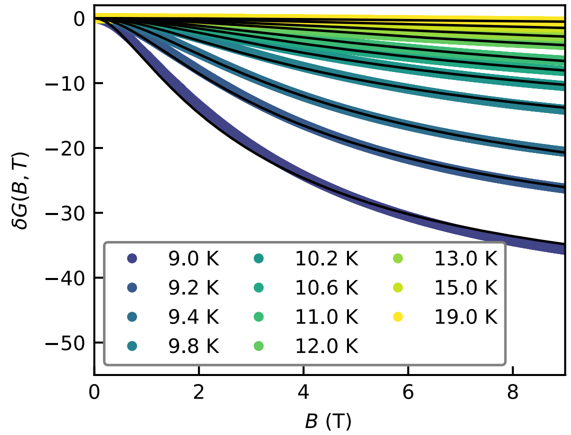

FIG. 4. Dimensionless magnetoconductance vs magnetic field for a set of fixed temperatures indicated in the legend for the representative NbTiN film with a thickness of 6 nm. Symbols: experimental data; black curves: the best fits with a sum of Eqs. (A1)–(A4).

The experimental dependence $\tau_\phi^{-1}(T)$ is described with a sum of rates affiliated with different phase-breaking scattering

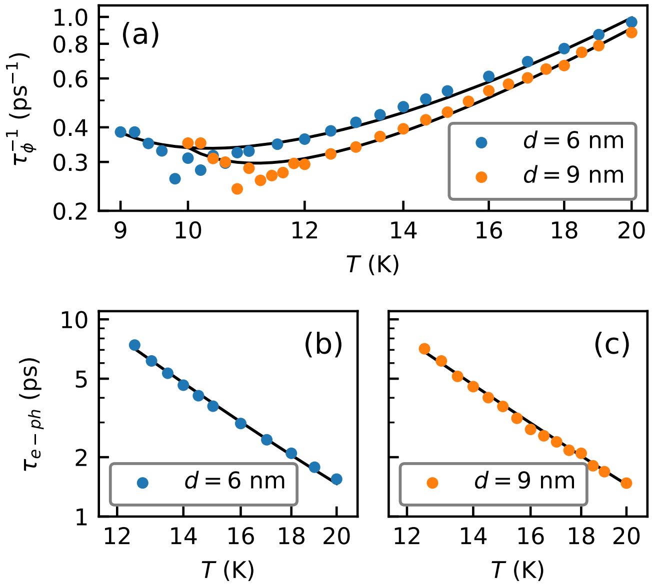

FIG. 5. (a) Electron dephasing rate vs temperature. Symbols: the best-fit values of $\tau_\phi^{-1}(T)$ obtained by fitting the experimental $\delta G(B, T)$ data; solid curves: the best fits with Eq. (2). Electron-phonon scattering time vs temperature for the NbTiN film with (b) $d = 6$ nm and (c) $d = 9$ nm in a double-logarithmic scale. Symbols: values of $\tau_{e\text{-ph}}(T)$ obtained from the experimental τ_ϕ^{-1} data as $\tau_{e\text{-ph}} = (\tau_\phi^{-1} - \tau_{e-e}^{-1} - \tau_{e-fl}^{-1})^{-1}$; solid lines: the best fits with the SM model, Eqs. (B1a) and (B1b).

TABLE II. Some of the electron- and phonon-related parameters of the NbTiN films studied here and films from two other materials (NbN and WSi) for comparison. The values of u_t and ρ are obtained from fits with the SM model. The values of τ_{esc} and c_e/c_{ph} are obtained from fits with the 2-T model.

Film	Sample	$\alpha_{e\text{-ph}}$[a] (ps)	n[b]	$\tau_{e\text{-ph}}(10\text{ K})$[c] (ps)	$\tau_{\text{EP}}(T_{C0})$[d] (ps)	τ_{esc} (ps)	$c_e/c_{\text{ph}}(T_{C0})$
NbTiN	L135	31.2 ± 3.5	3.5 ± 0.1	16.9	4.9	52.6 ± 1.5	0.39 ± 0.04
NbTiN	L134	17.7 ± 1.1	3.4 ± 0.1	15.0	2.9	79.6 ± 4.3	0.13 ± 0.01
NbN [12]	2559	9.3	3.5	11.9	1.4	25.9	0.83 ± 0.18
NbN [12]	A853	21.7	3.2	12.4	4.2	39.0	0.25 ± 0.03
WSi [16]	4	66	3.0	4.5	14.9	-	1.40 ± 0.30

[a] At $T = T_{C0}$, $\tau_{e\text{-ph}}$ equals $\alpha_{e\text{-ph}}$.

[b] The exponent in the temperature dependence of $\tau_{e\text{-ph}}^{-1} \propto T^n$.

[c] The dephasing time due to *e*-ph scattering (identical to the single-particle *e*-ph scattering time [31]) extrapolated to 10 K.

[d] The *e*-ph energy relaxation time (proportional to $\tau_{e\text{-ph}}$ with the proportionality coefficient computed with Eq. (11) in [32]).

events in which electrons are involved. In the absence of extrinsic phase-breaking sources, these are electron-electron (*e*-*e*) [28], electron-phonon (*e*-ph) [29], and electron-fluctuation (*e*-fl) [30] scattering events. Consequently,

$$\tau_\phi^{-1} = \tau_{e\text{-}e}^{-1} + \tau_{e\text{-ph}}^{-1} + \tau_{e\text{-fl}}^{-1}, \qquad (2)$$

where

$$\tau_{e\text{-}e}^{-1} = \frac{k_B T}{\hbar} \frac{1}{2C_1} \ln(C_1), \qquad (2a)$$

$$\tau_{e\text{-ph}}^{-1} = \alpha_{e\text{-ph}}^{-1} (T/T_{C0})^n, \qquad (2b)$$

$$\tau_{e\text{-fl}}^{-1} = \frac{k_B T}{\hbar} \frac{1}{2C_1} \frac{2\ln(2)}{\ln(T/T_{C0}) + C_2}. \qquad (2c)$$

Here, $C_1 = \pi\hbar/(R_{\text{SN}} e^2)$ and $C_2 = 4\ln(2)/[\sqrt{\ln(C_1)^2 + 128 C_1/\pi} - \ln(C_1)]$. The expression for the *e*-*e* dephasing rate, Eq. (2a), accounts for only dephasing due to Nyquist noise, which dominates in our experimental temperature range $T \ll \hbar/(k_B \tau_e) \sim 10^4$ K [$\tau_e = l_e^2/(3D) = 0.3$ and 0.5 fs for NbTiN films with thicknesses of 6 and 9 nm, respectively]. It is worth noting that the expression for the *e*-ph dephasing rate, Eq. (2b), is valid in a relatively small temperature range where n is constant; in general, n varies with the temperature. We fitted the experimental $\tau_\phi^{-1}(T)$ data shown in Fig. 5(a) with Eq. (2) using two independent fitting parameters, $\alpha_{e\text{-ph}}$ and n. At T_{C0}, $\tau_{e\text{-ph}}$ equals $\alpha_{e\text{-ph}}$. The best-fit values of $\alpha_{e\text{-ph}}$ and n are listed in Table II, together with $\tau_{e\text{-ph}}$ values extrapolated to 10 K.

Figures 5(b) and 5(c) show $\tau_{e\text{-ph}}$ obtained from the dephasing rates as $\tau_{e\text{-ph}} = (\tau_\phi^{-1} - \tau_{e\text{-}e}^{-1} - \tau_{e\text{-fl}}^{-1})^{-1}$ in the temperature range where $\tau_{e\text{-ph}}^{-1}$ dominates other dephasing rates. In the dirty limit with respect to *e*-ph scattering characterized by the product $q_T l_e \ll 1$, where $q_T = k_B T/\hbar u$ is the phonon wave vector and u is the sound velocity, *e*-ph scattering is described by a model developed by Sergeev and Mitin [29] (the SM model; see Appendix B). The model provides the single-particle *e*-ph scattering time, which is identical to $\tau_{e\text{-ph}}$ [31] extracted with the magnetoconductance method. We fitted experimental $\tau_{e\text{-ph}}$ data with the SM model, Eq. (B1), using two independent fitting parameters: the sound velocity of transverse phonons u_t and the mass density ρ. We fixed other parameters such as k_F, l_e, and $N(0)$ to their values given in Table I and adopted for m_e the value of the free-electron mass. We implemented the lattice parameter $a_0 = 0.43$ nm [33–35], the sound velocity of longitudinal phonons $u_l = 2u_t$ that is approximately valid for a large variety of materials, and $k \sim 1.0$ (Appendix B). The best-fit values of u_t and ρ are listed in Table III.

C. Photoresponse in the time domain

We studied the energy relaxation of nonequilibrium electrons in NbTiN microbridges by means of the photoresponse technique. The microbridges with the geometry sketched in Fig. 6 were fabricated from the two NbTiN films with thicknesses of 6 and 9 nm, shaped to a width of ~90 μm and a length of ~1 μm (along the current flow) with tapered contacts toward the electrodes to reduce the current-crowding effect. The microbridges were installed in a continuous-flow cryostat, kept in the resistive state at an ambient temperature

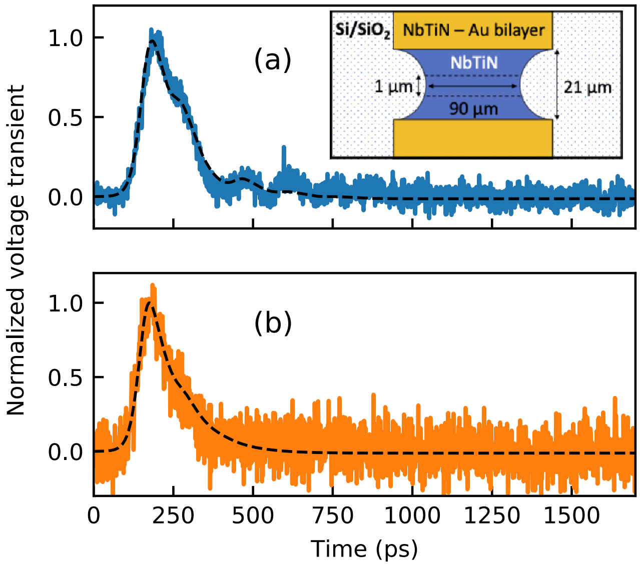

FIG. 6. Normalized voltage transient vs time for microbridges fabricated from the NbTiN film with (a) $d = 6$ nm and (b) $d = 9$ nm. Solid curves: experimental data; dashed curves: the best fits with the 2T model, Eqs. (9)–(13) in [12]. The inset is a sketch of the microbridge geometry.

TABLE III. Phonon-related properties. c^*_{ph} and c_{ph} were computed as for 3D Debye at a critical temperature of a corresponding film and using sound velocities u^* and u, respectively. $c^{\mathrm{exp}}_{\mathrm{ph}}$ were obtained from c_e/c_{ph} ratios found as the best fits of the 2T model to the photoresponse data with c_e predicted by the Drude model.

Film	Sample	u^{*}_{t} [a] (nm/ps)	u^{*}_{l} [a] (nm/ps)	ρ^{*} [a] (g/cm^3)	c^{*}_{ph} (J/Km^3)	u_t [b] (nm/ps)	ρ [b] (g/cm^3)	c_{ph} (J/Km^3)	$c^{\mathrm{exp}}_{\mathrm{ph}}$ (J/Km^3)
NbTiN	L135	5.3–4.7	9.0–8.4	6.7–7.5	400–500	1.8	3.0	8800	2700
NbTiN	L134	5.3–4.7	9.0–8.4	6.7–7.5	500–700	1.9	3.6	10800	11000
NbN [12]	2259	4.4	8.0	8.2	1300	2.4	7.8	7800	2500
NbN [12]	A853	4.4	8.0	8.2	600	2.2	5.2	4700	4000
WSi [16]	4	3.0	5.4	15.8	200	2.1[c]	8.2[c]	630	560

[a] Computed from first principles for NbTiN [34], NbN [34], and W_3Si [39] with crystalline structures.

[b] Best-fit values of the parameters in the SM model.

[c] Obtained in Appendix C.

slightly larger than T_{C0}, and exposed to light pulses via a quartz window of the cryostat. Light was focused onto the microbridges into a spot with a diameter larger than ~100 μm. The light pulses were generated by a Ti:sapphire laser at a wavelength of about 800 nm with a repetition rate of 80 MHz and subpicosecond duration. Biasing the microbridges with a small direct current, we recorded their photoresponse (amplified voltage transients) to light pulses in the time domain with a sampling oscilloscope (Fig. 6). The overall bandwidth of our readout was 0.1–5 GHz.

There are other optical methods to probe ultrafast dynamics of electrons, e.g., the pump-probe technique [36], second-harmonic generation [37], and two-photon emission [38]. They, however, reveal dynamics at high energies (≈1 eV) due to interaction with optical phonons.

We described the voltage transients, shown in Fig. 6, with the two-temperature (2T) model using the formalism given by Eqs. (9)–(13) in [12]. This formalism takes into account the effect of a finite readout bandwidth and the signal ringing caused by impedance mismatch. The latter is seen in Fig. 6(a). The 2T model describes the evolution of electron and phonon effective temperatures raised by excitation via two coupled time-dependent equations with three independent parameters: the ratio between electron and phonon heat capacities c_e/c_{ph}, the phonon escape time τ_{esc}, and the *e*-ph energy relaxation time τ_{EP}. We note here that τ_{EP} differs from $\tau_{e\text{-ph}}$ (both are listed for each film in Table II) by a coefficient $\mu = \tau_{\mathrm{EP}}/\tau_{e\text{-ph}} < 1$, given by Eq. (11) in [32], which depends on the exponent n, e.g., $\mu \approx 0.6$ for $n = 2.0$ and $\mu \approx 0.1$ for $n = 4.0$. Hence, describing the photoresponse with the 2T model, one gets indirect *calorimetric* information about heat capacities.

We fitted the experimental transients using c_e/c_{ph} and τ_{esc} as fitting parameters, along with the fixed values of τ_{EP}. The results are shown in Fig. 6. The best-fit values of c_e/c_{ph} and τ_{esc}, together with computed values of τ_{EP}, are listed in Table II.

III. DISCUSSION

We start by comparing rates of *e*-ph scattering in the NbTiN films studied here and the parent compounds of NbTiN, NbN and TiN. For NbTiN films, we found $1/\tau_{e\text{-ph}} \propto T^{3.45\pm0.05}$ in the temperature range from 12 to 20 K and the magnitude of $\tau_{e\text{-ph}}(T)$ extrapolated to 10 K, $\tau_{e\text{-ph}}(10K) = 16 \pm 1$ ps. $1/\tau_{e\text{-ph}} \propto T^{3.0}$ was found for thin TiN films in the temperature range from 1.7 to 4.2 K [11], resulting in $\tau_{e\text{-ph}}(10\text{ K}) \sim 1800$ ps (actually, the authors derived the *e*-ph energy relaxation time, τ_{EP} in our notation, which we used along with the exponent n to estimate $\tau_{e\text{-ph}}$). For NbN films, $1/\tau_{e\text{-ph}} \propto T^{3.5\pm0.3}$ was found in the temperature range from 14 to 30 K along with the extrapolated value $\tau_{e\text{-ph}}(10\text{ K}) = 15 \pm 3$ ps [12]. As clearly seen in Fig. 7, with respect to inelastic *e*-ph interaction, our $Nb_xTi_{1-x}N$ films with $x \approx 0.6$ are closer to NbN than to TiN. This certainly indicates that the stoichiometry of $Nb_xTi_{1-x}N$ cannot be used for fine-tuning the *e*-ph scattering rate in this compound.

Let us now discuss the magnitude of the $\tau_{e\text{-ph}}$ provided by the SM model (Appendix B). Under the condition $q_T l_e \ll 1$ and the dominance of vibrating scattering centers ($k \sim 1$) fulfilled for our films, $\tau_{e\text{-ph}(l)} \gg \tau_{e\text{-ph}(t)}$, and consequently, the total rate is controlled by the interaction of electrons with transverse phonons, i.e., $\tau_{e\text{-ph}} \equiv \tau_{e\text{-ph}(t)}$. Therefore, we can limit the qualitative discussion to the properties of transverse phonons (in quantitative estimations we account for all phonon polarizations, one longitudinal and two transversal). Interacting with a phonon, an electron exchanges momentum $\sim q_T$ within an interaction region $\sim 1/q_T \propto u_t$, so that the smaller the phonon velocity is, the smaller the interaction region is, and the shorter the interaction time is. In fact, $\tau_{e\text{-ph}(t)} \propto \rho u_t^3$ [Eq. (B1b)]. Feeding the SM model with

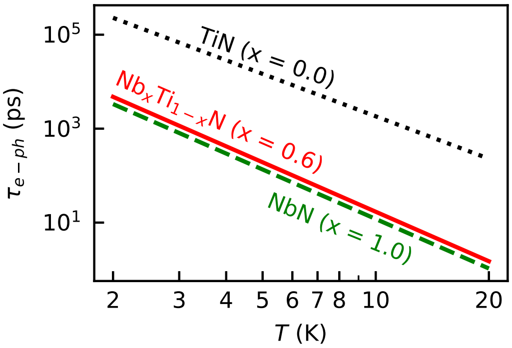

FIG. 7. The *e*-ph scattering time vs temperature for different Nb fractions in the $Nb_xTi_{1-x}N$ compound. The data for NbN and NbTiN were extrapolated to temperatures below 10 K, and those for TiN were extrapolated to temperatures above 4 K (see the main text).

properties of bulk crystalline NbTiN ($\rho^* = 7.5$ g/cm^3 and $u_t^* = 4.7$ nm/ps [34]) results in enormously large $\tau_{e\text{-ph}}$ compared to the experimental value obtained from magnetoconductance (Table II).

Thus, we used ρ and u_t in the SM model as fitting parameters. We applied the same procedure to fit the $\tau_{e\text{-ph}}$ data obtained for thin WSi films by magnetoconductance measurements in [16] (see Appendix C). The best-fit values of u_t and ρ for NbTiN and WSi films are listed in Table III.

Let us now estimate the phonon escape time using the acoustic mismatch model [40]. First, we compute the transmission $\bar{\eta} \approx 0.2$ of the film/substrate interface for phonons using the best-fit values of u_t and ρ (see Table III for our NbTiN films; for the SiO$_2$ substrate, we took the values from Table I in [40]). Further, we find $\tau_{\text{esc}} = 4d/(\bar{\eta}\bar{u}) \approx 60.6$ ps for the film with $d = 6$ nm and 81.9 ps for the film with $d = 9$ nm, where $\bar{u} \approx u_t$ is the weighted sound velocity. Calculation details for $\bar{\eta}$ and $\bar{u}$ are reported in [12]. Hence, in NbTiN films the phonon escape time scales with the film thickness as τ_{esc} (ps) $\approx 9d$ (nm). The computed values of τ_{esc} are in good agreement with those found as best fits to the photoresponse data in the framework of the 2T model (Table II). This allows us to conclude that the SM model provides reasonable values of u_t and ρ.

Further, from the best-fit c_e/c_{ph} ratios (Table II) and $c_e = \pi^2 k_B^2 N(0) T/3$ predicted by the Drude model, we find the phonon heat capacities $c_{\text{ph}}^{\text{exp}}$, which are listed in Table III. Here, we assume that the Drude model predicts the correct value of c_e, relying on the fact that our NbTiN films are three-dimensional (3D) with respect to electron transport ($d \gg l_e$).

It is clearly seen from Table III that the best-fit values of u_t for thin NbTiN, NbN, and WSi films are systematically reduced compared to those of corresponding bulk crystalline materials (marked with an asterisk in Table III) by $(u_t^* - u_t)/u_t^* \sim 40\%$–$60\%$. Moreover, for all these films, both experimental (calorimetric) $c_{\text{ph}}^{\text{exp}}$ and c_{ph} computed in the framework of the Debye model for 3D phonons with the reduced sound velocities as $c_{\text{ph}} = 2/5\,\pi^2 k_B (k_B T/\hbar)^3 u_{av}^{-3}$, where $u_{av} = [2/3u_t^{-3} + 1/3u_l^{-3}]^{-1/3} \approx u_t$, are systematically larger than the heat capacities c_{ph}^* computed within the same approximation with the sound velocities of corresponding bulk crystalline materials.

There are three effects on the sound velocity and phonon heat capacity to discuss: (i) phonon softening, (ii) film morphology (amorphous or granular structure), and (iii) depletion of long-wavelength phonon states in grains or thin films.

In a thin monocrystalline film, phonon softening, i.e., the decrease in the effective Debye temperature with respect to the bulk value, occurs due to weakening of ion bonds at film surfaces [41]. Grain boundaries and defects increase the relative number of weak bonds and enhance phonon softening. [42,43]. Clearly, the weakening of bonds leads to a reduction in the mean sound velocity and a corresponding increase in the phonon heat capacity. The effect is most pronounced in ultrathin granular films due to a large surface-to-volume ratio. We have to note here that an alternative explanation of this effect relying on the proximity effect between the film and the oxide layers on the film surfaces exists [44].

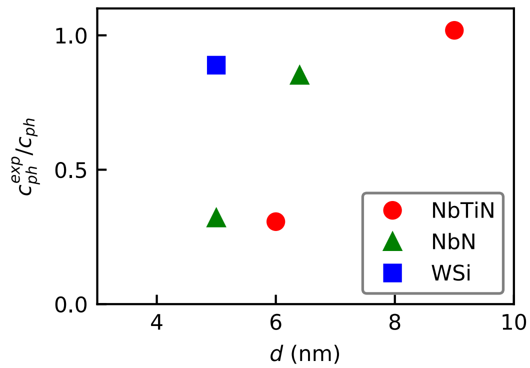

FIG. 8. Ratio of experimental (calorimetric) and Debye phonon heat capacities.

The structure of both NbTiN films [18] and NbN films [44–46] is polycrystalline and granular, with the mean grain size of the order of the film thickness or larger. Polycrystalline NbTiN and NbN films are composites of crystalline grains with amorphous boundaries [47], while WSi films are rather amorphous (verified by x-ray diffraction in 60-nm-thick WSi films [48]) without pronounced grains. However, it was recently shown that 6-nm-thick WSi films exhibit a preferred orientation rather than an amorphous state [49]. For longitudinal phonons, the amorphous phase is not expected to reduce noticeably the sound velocity, while for transverse phonons it does because of substantial weakening of shear modulus. A large reduction of transverse sound velocities in amorphous materials, relative to the crystalline materials, was observed, for instance, in [50]. This effect can be considered amorphous phonon softening. It results in an increase in the phonon heat capacity by the factor $c_{\text{ph}} \propto u_t^{-3}$ [51] controlled by the reduction of the sound velocity in an amorphous state compared to the crystalline material.

At low temperatures, the wavelength of a thermal phonon $\lambda_{\text{ph}} \approx 2\pi\hbar u/(k_B T)$ becomes comparable to or larger than the film thickness. This modifies the 3D Debye phonon spectrum in such a way that the phonon states are empty (or depleted) for phonons with wave vectors perpendicular to the film plane and smaller than $q_{\min} = \pi/d$. The size effect on phonon spectra in metallic films with variable thicknesses on a semi-infinite substrate was computed and compared with experimental data at low temperatures in [52]. For phonons excited perpendicular to the film/substrate interface, the authors found a strong depletion of long-wavelength phonon states beyond the cutoff wavelength $\lambda_{\max} = 2d$. Qualitatively, the depletion should not affect the sound velocity and should cause only a reduction in the phonon heat capacity; its impact should grow with the ratio λ_{ph}/d. For granular films a similar, but even stronger, effect exists. When λ_{ph} exceeds the grain size, the depletion is almost isotropic; that is, it affects phonon states in all directions of the wave vector. Hence, the impact of depletion on the phonon heat capacity depends on both the film thickness and the film morphology.

In Fig. 8, we plot the ratio r of the experimental (calorimetric) phonon heat capacities $c_{\text{ph}}^{\text{exp}}$ and the values, c_{ph}, computed for 3D Debye phonons with reduced sound velocities u_t of the SM model (Table III). The data group around two values: (1) $r \approx 0.4$ for films with reduced $c_{\text{ph}}^{\text{exp}}$ and (2) $r \approx 1$ for films with $c_{\text{ph}}^{\text{exp}}$ close to the Debye value. Both films with reduced

$c_{\rm ph}^{\rm exp}$ (NbTiN with $d = 6$ nm and NbN with $d = 5$ nm) are granular, with a grain size of the order of the film thickness. Hence, the most plausible explanation for the reduction in phonon heat capacity is the depletion of long-wavelength phonon states in grains. The data for the second group belong to either an amorphous thin film (WSi film with $d = 4$ nm) or granular thicker films (NbTiN with $d = 9$ nm and NbN with $d = 6.4$ nm). Sticking to the interpretation of the data from the first group, we have to conclude that the depletion of long-wavelength phonon states in these films is less pronounced. For thin amorphous films, the depletion is less than that of granular films of the same thickness because only phonon states with wave vectors perpendicular to the film plane are depleted (as we discussed above). For thicker granular NbN and NbTiN films, an expected [18,44–46] increase in the grain size, following the increase in the film thickness, relaxes the impact of depletion on the phonon heat capacity. In contrast to free grains, grain surfaces in our films are clamped. Therefore, depletion of long-wavelength phonon states in our films is expected to cause a decrease in the heat capacity with the decrease of the grain size [53]. Our results support these expectations.

Another important observation is that for all thin films reported here, the best-fit values of mass densities (ρ in Table III) are noticeably lower than those computed from known sizes of unit cells for corresponding crystalline materials (ρ^* in Table III and references cited therein). We believe that the difference is the direct consequence of the film morphology since in an amorphous or polycrystalline film host atoms are packed at a lower density than in the corresponding crystalline material.

Finally, let us compare the properties of our NbTiN films and NbN films studied in [12] (samples 2259 and A853) that are relevant to SNSPD and HEB practical devices. With respect to superconducting and transport properties, together with e-ph scattering times, both materials are very similar. The main difference is in their phonon escape times; in NbTiN/SiO$_2$ (this study) $\tau_{\rm esc}$ (ps) $\approx 9d$ (nm) is about twice as large as in NbN/SiO$_2$ [$\tau_{\rm esc}$ (ps) $\approx 5d$ (nm)] [12]. Besides the timing jitter, the difference in $\tau_{\rm esc}$ is not expected to noticeably affect the performance of an SNSPD. However, this difference severely affects the performance of a HEB. Specifically, its IF bandwidth is controlled by the cooling rate of electrons, in which the phonon escape rate plays a limiting role [8,9]. A larger $\tau_{\rm esc}$ results in a smaller IF bandwidth. This explains why, despite all efforts, NbTiN-based HEBs repeatedly demonstrate smaller IF bandwidth than NbN-based HEBs [2].

IV. CONCLUSION

We have studied dephasing and energy relaxation of electrons in thin superconducting NbTiN films on Si/SiO$_2$ substrates with magnetoconductance and photoresponse techniques, respectively, and compared our results with those reported in the literature for NbN and WSi films. Our main findings are the following:

(1) The studied NbTiN films are strongly disordered with respect to electron-phonon scattering, the product $q_T l_e(T_C) \ll 1$, electron transport, and the Ioffe-Regel parameter $k_F l_e = 2.5$–3.0. In the temperature range from 12 to 20 K, their inelastic e-ph scattering rate varies as $\tau_{e\text{-ph}}^{-1} \propto T^n$, with $n = 3.4$–3.5, and amounts (extrapolated) to 15.0–16.9 ps at 10 K. The phonon escape time varies with the film thickness as $\tau_{\rm esc}$ (ps) $\approx 9d$ (nm).

(2) In all studied and considered films, we have found a systematic reduction of the sound velocity by $\Delta u/u = 40\%$–60% compared to the sound velocities computed from first principles for corresponding bulk crystalline materials.

(3) For all films the experimental calorimetric heat capacities of phonons are much larger than the heat capacities computed for corresponding crystalline materials with the 3D Debye model. This is most likely due to phonon softening. For thin polycrystalline granular films calorimetric heat capacities are a few times less than those computed with the reduced sound velocities using the 3D Debye model. This is most likely due to the depletion of long-wavelength phonon states in grains.

ACKNOWLEDGMENTS

The authors greatly acknowledge the help of V. Zwiller in the sample preparation and stimulating discussions with K. Illin on the magnetic properties and morphology of superconducting granular films.

APPENDIX A: QUANTUM CORRECTIONS

The theory of quantum corrections to the classical Drude conductance is applicable for materials with $k_F l_e > 1$. With respect to the characteristic scales of the theory, i.e., the thermal coherence length $L_T = \sqrt{2\pi\hbar D/(k_B T)}$ and the electron dephasing length L_ϕ, our NbTiN films belong to quasi-2D systems ($d < L_T, L_\phi$). Therefore, the analytical expressions we use to compute theoretical (dimensionless) corrections correspond to the 2D limit. For weak spin-orbit interaction and in the absence of magnetic scattering, the WL correction [24,54] is given by

$$\delta G^{\rm WL}(B,T) = \frac{3}{2} Y\left(\frac{B}{\frac{4}{3}B_{\rm so} + B_\phi}\right) - \frac{1}{2} Y\left(\frac{B}{B_\phi}\right). \qquad \text{(A1)}$$

Here, the function $Y(x) = \ln(1/x) + \psi(1/2 + 1/x)$ is defined via the digamma function $\psi(x)$. The characteristic fields are defined as $B_j = \hbar/(4eD\tau_j)$, where the indices so and ϕ stand for spin-orbit and dephasing scattering, respectively. The AL correction [19] is given by

$$\delta G^{\rm AL}(B,T) = \frac{\pi^2}{2\ln(T/T_{C0})}\left(\frac{B_C}{B}\left\{1 - 2\frac{B_C}{B}\left[\psi\left(1 + \frac{B_C}{B}\right) - \psi\left(\frac{1}{2} + \frac{B_C}{B}\right)\right]\right\} - \frac{1}{4}\right). \qquad \text{(A2)}$$

Here, $B_C = C^* \hbar/(4eD\tau_{\mathrm{GL}})$, where the Ginzburg-Landau time $\tau_{\mathrm{GL}} = (\pi\hbar)/[8k_B T \ln(T/T_{C0})]$ represents the lifetime of Cooper pairs. The MT correction [20,21,55,56] is given by

$$\delta G^{\mathrm{MT}}(B, T) = -\beta_{\mathrm{LSA}}(T)\left[Y\left(\frac{B}{B_\phi}\right) - Y\left(\frac{B}{B_C}\right)\right], \tag{A3}$$

where the parameter $\beta_{\mathrm{LSA}}(T) = 2\pi k_B T \hbar^{-1}(1/\tau_{\mathrm{GL}} - 1/\tau_\phi)^{-1}$. Finally, the DOS correction [22,57] is given by

$$\delta G^{\mathrm{DOS}}(B, T) = \frac{28\varsigma(3)}{\pi^2} Y\left(\frac{B}{B_C}\right), \tag{A4}$$

where $\varsigma(3) = 1.202$ is the Riemann zeta function. The total theoretical magnetoconductance, i.e., the sum of the four terms in Eqs. (A1)–(A4), is used to describe the experimental $\delta G(B, T)$ data.

APPENDIX B: INELASTIC *e*-PH (SINGLE-PARTICLE) SCATTERING TIME

The degree of disorder with respect to *e*-ph scattering is characterized by the product $q_T l_e$. For our NbTiN films, in the experimental temperature range, $q_T l_e \ll 1$, which corresponds to the strong disordered regime. The SM model [29] describes *e*-ph scattering in disordered metals and provides the inelastic (single-particle) scattering rate of electrons at the Fermi level via interaction with phonons of different polarizations:

$$\tau_{e\text{-ph}}^{-1} = \tau_{e\text{-ph}(l)}^{-1} + \tau_{e\text{-ph}(t)}^{-1}, \tag{B1}$$

where interaction with *longitudinal* phonons is accounted for in

$$\tau_{e\text{-ph}(l)}^{-1} = \frac{7\pi\zeta(3)}{2\hbar} \frac{\beta_l (k_B T)^3}{(p_F u_l)^2} F_l(q_{T(l)} l_e) \tag{B1a}$$

and that with *transverse* phonons (two polarizations are taken into account) is accounted for in

$$\tau_{e\text{-ph}(t)}^{-1} = 3\pi^2 \frac{\beta_t (k_B T)^2}{(p_F u_t)(p_F l_e)} k F_t(q_{T(t)} l_e). \tag{B1b}$$

The indices l and t denote values associated with phonons of longitudinal and transverse polarizations. Here, $\beta_{l(t)} = (2E_F/3)^2[N(0)/(2\rho u_{l(t)}^2)]$ is the dimensionless coupling constant, $E_F = (p_F)^2/(2m_e)$ is the Fermi energy, $p_F = \hbar k_F$ is the Fermi momentum, and m_e is the electron mass. In Eq. (B1a), the integral $F_l(z) = \frac{2}{7\zeta(3)} \int_0^{A_l} dx\, \Phi_l(xz)[N(x) + n(x)]x^2$, where $N(x)$ and $n(x)$ are Bose and Fermi distribution functions and $\Phi_l(x) = \frac{2}{\pi}(\frac{x \arctan(x)}{x - \arctan(x)} - \frac{3}{x}k)$ is the Pippard function. In Eq. (B1b), the integral $F_t(z) = \frac{4}{\pi^2} \int_0^{A_t} dx\, \Phi_t(xz)[N(x) + n(x)]x$, where $\Phi_t(x) = 1 + k[3x - 3(x^2 + 1)\arctan(x)]/[2x^3]$. The upper limit of the integrals $F(z)$ is $A_{l(t)} = (6\pi^2)^{1/3}(a_0\, q_{T,l(t)})^{-1}$. The parameter $1 \geqslant k \geqslant 0$ reveals the property of electron scattering centers ($k = 1$ corresponds to scattering centers vibrating in the same way as the host lattice, e.g., light impurities; $k = 0$ corresponds to the static scattering centers, e.g., heavy impurities and rigid boundaries).

The total inelastic *e*-ph scattering rate given by Eq. (B1) is used to describe the experimental $\tau_{e\text{-ph}}$ data shown in Figs. 5(a) and 5(b).

APPENDIX C: WSI FILMS

We describe the $\tau_{e\text{-ph}}(T)$ data obtained with the magnetoconductance method for WSi films in [16] using the SM model (Appendix B). Following the notation here, the authors of [16] found $\alpha_{e\text{-ph}} \equiv \tau_{e\text{-ph}}(T_{C0}) = 66$ ps and $n = 3$ between 5 and 20 K, which we added to Table II. Fitting the SM model to these data, we used two independent parameters, u_t and ρ; other parameters such as D and $N(0)$ were fixed at the values provided in [16] (also listed in Table I). We used $a_0 = 0.46$ nm [58], $k_F = N(0)\pi^2\hbar^2/m_e$ computed with the free-electron mass m_e, $l_e \sim 0.2$ nm, and $k \sim 1.0$. The best-fit values of u_t and ρ are listed in Table III.

[1] I. Esmaeil Zadeh, J. Chang, J. W. Los, S. Gyger, A. W. Elshaari, S. Steinhauer, S. N. Dorenbos, and V. Zwiller, Superconducting nanowire single-photon detectors: A perspective on evolution, state-of-the-art, future developments, and applications, Appl. Phys. Lett. **118**, 190502 (2021).

[2] A. Shurakov, Y. Lobanov, and G. Goltsman, Superconducting hot-electron bolometer: From the discovery of hot-electron phenomena to practical applications, Supercond. Sci. Technol. **29**, 023001 (2015).

[3] R. Barends, N. Vercruyssen, A. Endo, P. De Visser, T. Zijlstra, T. Klapwijk, P. Diener, S. Yates, and J. Baselmans, Minimal resonator loss for circuit quantum electrodynamics, Appl. Phys. Lett. **97**, 023508 (2010).

[4] N. Samkharadze, A. Bruno, P. Scarlino, G. Zheng, D. P. DiVincenzo, L. DiCarlo, and L. M. K. Vandersypen, High-Kinetic-Inductance Superconducting Nanowire Resonators for Circuit QED in a Magnetic Field, Phys. Rev. Appl. **5**, 044004 (2016).

[5] D. J. Van Woerkom, A. Geresdi, and L. P. Kouwenhoven, One minute parity lifetime of a NbTiN Cooper-pair transistor, Nat. Phys. **11**, 547 (2015).

[6] M. Burdastyh, S. Postolova, T. Proslier, S. Ustavshikov, A. Antonov, V. Vinokur, and A. Y. Mironov, Superconducting phase transitions in disordered NbTiN films, Sci. Rep. **10**, 1471 (2020).

[7] A. Y. Mironov, D. M. Silevitch, T. Proslier, S. V. Postolova, M. V. Burdastyh, A. K. Gutakovskii, T. F. Rosenbaum, V. V. Vinokur, and T. I. Baturina, Charge Berezinskii-Kosterlitz-Thouless transition in superconducting NbTiN films, Sci. Rep. **8**, 4082 (2018).

[8] A. D. Semenov, G. N. Gol'tsman, and R. Sobolewski, Hot-electron effect in superconductors and its applications for radiation sensors, Supercond. Sci. Technol. **15**, R1 (2002).

[9] T. M. Klapwijk and A. Semenov, Engineering physics of superconducting hot-electron bolometer mixers, IEEE Trans. Terahertz Sci. Technol. **7**, 627 (2017).

[10] D. Y. Vodolazov, Minimal Timing Jitter in Superconducting Nanowire Single-Photon Detectors, Phys. Rev. Appl. **11**, 014016 (2019).

[11] A. Kardakova, M. Finkel, D. Morozov, V. Kovalyuk, P. An, C. Dunscombe, M. Tarkhov, P. Mauskopf, T. Klapwijk, and G. Goltsman, The electron-phonon relaxation time in thin superconducting titanium nitride films, Appl. Phys. Lett. **103**, 252602 (2013).

[12] M. Sidorova, A. Semenov, H.-W. Hübers, K. Ilin, M. Siegel, I. Charaev, M. Moshkova, N. Kaurova, G. N. Goltsman, X. Zhang, and A. Schilling, Electron energy relaxation in disordered superconducting NbN films, Phys. Rev. B **102**, 054501 (2020).

[13] A. D. Semenov, Superconducting nanostrip single-photon detectors some fundamental aspects in detection mechanism, technology and performance, Supercond. Sci. Technol. **34**, 054002 (2021).

[14] H. Le Jeannic, V. B. Verma, A. Cavaillès, F. Marsili, M. D. Shaw, K. Huang, O. Morin, S. W. Nam, and J. Laurat, High-efficiency WSi superconducting nanowire single-photon detectors for quantum state engineering in the near infrared, Opt. Lett. **41**, 5341 (2016).

[15] V. B. Verma, B. Korzh, F. Bussières, R. D. Horansky, S. D. Dyer, A. E. Lita, I. Vayshenker, F. Marsili, M. D. Shaw, H. Zbinden, R. P. Mirin, and S. W. Nam, High-efficiency superconducting nanowire single-photon detectors fabricated from MoSi thin-films, Opt. Express **23**, 33792 (2015).

[16] X. Zhang, A. Engel, Q. Wang, A. Schilling, A. Semenov, M. Sidorova, H.-W. Hübers, I. Charaev, K. Ilin, and M. Siegel, Characteristics of superconducting tungsten silicide W_xSi_{1-x} for single photon detection, Phys. Rev. B **94**, 174509 (2016).

[17] S. Steinhauer, L. Yang, S. Gyger, T. Lettner, C. Errando-Herranz, K. D. Jöns, M. A. Baghban, K. Gallo, J. Zichi, and V. Zwiller, NbTiN thin films for superconducting photon detectors on photonic and two-dimensional materials, Appl. Phys. Lett. **116**, 171101 (2020).

[18] J. Zichi, J. Chang, S. Steinhauer, K. von Fieandt, J. W. N. Los, G. Visser, N. Kalhor, T. Lettner, A. W. Elshaari, I. E. Zadeh, and V. Zwiller, Optimizing the stoichiometry of ultrathin NbTiN films for high-performance superconducting nanowire single-photon detectors, Opt. Express **27**, 26579 (2019).

[19] L. Aslamasov and A. Larkin, The influence of fluctuation pairing of electrons on the conductivity of normal metal, Phys. Lett. A **26**, 238 (1968).

[20] K. Maki, Critical fluctuation of the order parameter in a superconductor. I, Prog. Theor. Phys. **40**, 193 (1968).

[21] R. S. Thompson, Microwave, flux flow, and fluctuation resistance of dirty type-II superconductors, Phys. Rev. B **1**, 327 (1970).

[22] A. Glatz, A. Varlamov, and V. Vinokur, Quantum fluctuations and dynamic clustering of fluctuating Cooper pairs, Europhys. Lett. **94**, 47005 (2011).

[23] G. M. Minkov, A. V. Germanenko, and I. V. Gornyi, Magnetoresistance and dephasing in a two-dimensional electron gas at intermediate conductances, Phys. Rev. B **70**, 245423 (2004).

[24] G. Bergmann, Quantum corrections to the resistance in two-dimensional disordered superconductors above T_C: Al, Sn, and amorphous $Bi_{0.9}Tl_{0.1}$ films, Phys. Rev. B **29**, 6114 (1984).

[25] M. H. Redi, Two-dimensional fluctuation-induced conductivity above the critical temperature, Phys. Rev. B **16**, 2027 (1977).

[26] E. Abrahams, R. Prange, and M. Stephen, Effect of a magnetic field on fluctuations above T_C, Physica (Amsterdam) **55**, 230 (1971).

[27] M. Tinkham, *Introduction to Superconductivity*, 2nd ed. (Dover Publications, Mineola, NY, 2004).

[28] B. L. Altshuler, A. Aronov, and D. Khmelnitsky, Effects of electron-electron collisions with small energy transfers on quantum localisation, J. Phys. C **15**, 7367 (1982).

[29] A. Sergeev and V. Mitin, Electron-phonon interaction in disordered conductors: Static and vibrating scattering potentials, Phys. Rev. B **61**, 6041 (2000).

[30] W. Brenig, M.-C. Chang, E. Abrahams, and P. Wölfle, Inelastic scattering time above the superconductivity transition in two dimensions: Dependence on disorder and magnetic field, Phys. Rev. B **31**, 7001 (1985).

[31] J. Rammer and A. Schmid, Destruction of phase coherence by electron-phonon interactions in disordered conductors, Phys. Rev. B **34**, 1352 (1986).

[32] K. Il'in, N. Ptitsina, A. Sergeev, G. Gol'tsman, E. Gershenzon, B. Karasik, E. Pechen, and S. Krasnosvobodtsev, Interrelation of resistivity and inelastic electron-phonon scattering rate in impure NbC films, Phys. Rev. B **57**, 15623 (1998).

[33] K. Makise, H. Terai, M. Takeda, Y. Uzawa, and Z. Wang, Characterization of NbTiN thin films deposited on various substrates, IEEE Trans. Appl. Supercond. **21**, 139 (2010).

[34] M. Arockiasamy, M. Sundareswari, and M. Rajagopalan, Ductility behaviour of cubic titanium niobium nitride ternary alloy: A first-principles study, Indian J. Phys. **90**, 149 (2016).

[35] D. Hazra, N. Tsavdaris, A. Mukhtarova, M. Jacquemin, F. Blanchet, R. Albert, S. Jebari, A. Grimm, A. Konar, E. Blanquet, F. Mercier, C. Chapelier, and H. Hofheinz, Superconducting properties of NbTiN thin films deposited by high-temperature chemical vapor deposition, Phys. Rev. B **97**, 144518 (2018).

[36] M. Ortolani, A. Mancini, A. Budweg, D. Garoli, D. Brida, and F. de Angelis, Pump-probe spectroscopy study of ultrafast temperature dynamics in nanoporous gold, Phys. Rev. B **99**, 035435 (2019).

[37] C. Guo, G. Rodriguez, and A. J. Taylor, Ultrafast Dynamics of Electron Thermalization in Gold, Phys. Rev. Lett. **86**, 1638 (2001).

[38] H. Petek and S. Ogawa, Femtosecond time-resolved two-photon photoemission studies of electron dynamics in metals, Prog. Surf. Sci. **56**, 239 (1997).

[39] Y. Pan and W. Guan, Probing the balance between ductility and strength: Transition metal silicides, Phys. Chem. Chem. Phys. **19**, 19427 (2017).

[40] S. B. Kaplan, Acoustic matching of superconducting films to substrates, J. Low Temp. Phys. **37**, 343 (1979).

[41] X. Lang and Q. Jiang, Finite size effect on critical transition temperature of superconductive nanosolids, Solid State Commun. **134**, 797 (2005).

[42] W. Ma, X. Zhang, and K. Takahashi, Electrical properties and reduced Debye temperature of polycrystalline thin gold films, J. Phys. D **43**, 465301 (2010).

[43] Z. Cheng, L. Liu, S. Xu, M. Lu, and X. Wang, Temperature dependence of electrical and thermal conduction in single silver nanowire, Sci. Rep. **5**, 1 (2015).

[44] A. Engel, A. Semenov, H.-W. Hübers, K. Il'in, and M. Siegel, Electric noise and local photon-induced nonequilibrium states in a current-carrying nanostructured superconductor, New Front. Supercond. Res. **6**, 153 (2006).

[45] K. Ilin, R. Schneider, D. Gerthsen, A. Engel, H. Bartolf, A. Schilling, A. Semenov, H.-W. Hübers, B. Freitag, and M. Siegel, Ultra-thin NbN films on Si: Crystalline and superconducting properties, J. Phys.: Conf. Ser., **97**, 012045 (2008).

[46] S.-Z. Lin, O. Ayala-Valenzuela, R. D. McDonald, L. N. Bulaevskii, T. G. Holesinger, F. Ronning, N. R. Weisse-Bernstein, T. L. Williamson, A. H. Mueller, M. A. Hoffbauer, M. W. Rabin, and M. J. Graf, Characterization of the thin-film NbN superconductor for single-photon detection by transport measurements, Phys. Rev. B **87**, 184507 (2013).

[47] H. Zhang, D. J. Srolovitz, J. F. Douglas, and J. A. Warren, Grain boundaries exhibit the dynamics of glass-forming liquids, Proc. Natl. Acad. Sci. USA **106**, 7735 (2009).

[48] B. Baek, A. E. Lita, V. Verma, and S. W. Nam, Superconducting a-W_xSi_{1-x} nanowire single-photon detector with saturated internal quantum efficiency from visible to 1850 nm, Appl. Phys. Lett. **98**, 251105 (2011).

[49] J. Jin, F. Fu, X. Jia, L. Kang, Z. Wang, X. Tu, L. Zhang, B. B. Jin, J. Chen, W. Xu, and P. Wu, Preparation and characterization of ultrathin WSi films for superconducting nanowire single-photon detectors, IEEE Trans. Appl. Supercond. **29**, 1 (2019).

[50] B. Golding, B. Bagley, and F. Hsu, Soft Transverse Phonons in a Metallic Glass, Phys. Rev. Lett. **29**, 68 (1972).

[51] G. Bergmann, Amorphous metals and their superconductivity, Phys. Rep. **27**, 159 (1976).

[52] W. Frick, D. Waldmann, and W. Eisenmenger, Phonon emission spectra of thin metallic films, Appl. Phys. **8**, 163 (1975).

[53] R. Lautehschläger, Improved theory of the vibrational specific heat of lead grains, Solid State Commun. **16**, 1331 (1975).

[54] S. Hikami, A. I. Larkin, and Y. Nagaoka, Spin-orbit interaction and magnetoresistance in the two dimensional random system, Prog. Theor. Phys. **63**, 707 (1980).

[55] A. Larkin, Reluctance of two-dimensional systems, JETP Lett. **31**, 219 (1980).

[56] J. M. B. Lopes dos Santos and E. Abrahams, Superconducting fluctuation conductivity in a magnetic field in two dimensions, Phys. Rev. B **31**, 172 (1985).

[57] A. Larkin and A. Varlamov, Fluctuation phenomena in superconductors, in *The Physics of Superconductors* (Springer, Berlin, Heidelberg, 2003), pp. 95–231.

[58] L. F. Mattheiss, Calculated structural properties of $CrSi_2$, $MoSi_2$, and WSi_2, Phys. Rev. B **45**, 3252 (1992).